# Rainbow scattering of argon from 2*H*-W(100)

Eli Pollak* and Jörg Tatchen
*Chemical Physics Department, Weizmann Institute of Science, 76100 Rehovoth, Israel*
(Received 24 June 2009; revised manuscript received 4 August 2009; published 3 September 2009)

The scattering of argon atoms from a hydrogen saturated tungsten (100) surface was measured almost two decades ago by Schweizer *et al.* [Surf. Sci. **249**, 335 (1991)]. Angular distributions with rainbow features were measured as a function of surface temperature, incident kinetic energy and incident angle. In this paper, we show that a recently formulated classical Wigner theory of atom surface scattering accounts well for the measured distributions and their properties. Parameters were fit to a corrugated Morse potential, with Ohmic friction. *Ab initio* quantum chemistry computations verify that the fitted Morse potential parameters are in qualitative agreement with computed Ar-W and Ar-*H*-W potentials of interaction.

DOI: 10.1103/PhysRevB.80.115404 PACS number(s): 34.35.+a, 34.50.−s, 61.05.Np, 68.49.Bc

## I. INTRODUCTION

The scattering of atoms and molecules from surfaces is seemingly well understood. So is the phenomenon of rainbow scattering. The vanishing of the derivative of the classical deflection function with respect to the impact parameter leads to peaks in measured angular distributions. In their 1991 review of rainbow scattering, Kleyn and Horn[1] note that the concept of rainbow scattering from surfaces was established forty years ago by McClure.[2] Given this long period of time and the fact that rainbow scattering from surfaces has been observed in many experiments,[3–12] and considered in various theoretical investigations,[11,13–20] one may well question the need for another theory paper on this topic.

Surprisingly, even though the fundamental physics underlying rainbow scattering is well understood,[1] experiments have raised many questions which remained unanswered as exemplified by the detailed investigation of the scattering of Ar from 2*H*-W(100). The measurements were made almost twenty years ago by Schweizer *et al.*,[10] but a quick search shows that their intriguing results have not been analyzed in any depth since then. They measured both diffraction and rainbows, here we concentrate on the rainbows, that is on the classical scattering. Their results were puzzling to them. They detected rainbow scattering at low incidence angles (−30°), but these disappeared when the incidence angle was increased to −60°, where the scattering was quasispecular. At low incidence angles the measured distribution was quite asymmetric about the specular angle, but the asymmetry became weaker as the energy of the incident particle was increased. At high incidence angles, the asymmetry disappeared. Not only have these qualitative puzzles remained unanswered to date, no one has attempted to fit their results to a simple classical model such as the washboard model of Tully.[16] The theory for interaction of a projectile with surface phonons and its effect on the scattering distribution, energy transfer, surface temperature effects is also a well-studied topic.[21–28] However, almost all papers have been limited to quasispecular scattering.

During the past few years we have developed a classical perturbation theory for the (in-plane) scattering of heavy atoms from surfaces. The theory includes both the effects of surface corrugation as well as interaction with surface phonons. In Ref. 29 we provided the perturbation theory framework and showed how the theory leads naturally to a description of rainbow scattering and its dependence on the angle of incidence and the surface temperature. We also compared the theory with numerically exact simulations and showed that it provides a reliable description of the scattering dynamics in the limit of weak corrugation. The theory was improved in Ref. 30, where the model used was explicitly translationally invariant and the theory was developed to include an analysis of the energy loss of the incident particle to the surface. In both these papers, the corrugation was treated in terms of a single sine $(\sin(\frac{2\pi x}{l}))$ (or cosine) term whose period was the lattice length $l$ of the surface. Such a description leads to symmetric scattering about the specular angle. In the third paper in the series[31] we showed that the noticeable asymmetry in the angular distribution measured in quite a few cases, may be attributed to the inclusion of a higher order Fourier component $(\sin(\frac{4\pi x}{l}))$. Analytic expressions were derived for the angular distribution in terms of a Morse potential model for the interaction of the incident atom in the vertical direction. This theory improved upon the washboard model of Tully,[16] since it is no longer necessary to consider only hard wall potentials.

The central theme of the present paper is to show that our classical perturbation theory may be used to model and explain the measured results for rainbow scattering of Ar from the hydrogen covered tungsten surface. We will show that a Morse potential for the vertical interaction with a well depth of 60 meV with weak corrugation and weak coupling to the phonon bath suffices for a full description of the experimentally measured results. We show that as the angle of incidence is increased, the distance between the rainbow angles decreases so that at high incidence angles, the coupling to the phonon bath "washes out" the rainbow structure and one remains with a single quasispecular peak. The rainbow angle distance decreases also as the incidence energy is increased, but the contribution of the second-order term in the Fourier expansion vanishes even faster leading to the disappearance of the asymmetry in the angular distribution.

For the sake of completeness, we review briefly in Sec. II the classical scattering theory as developed in Refs. 30 and 31. The analysis of the experimental results of Schweizer *et*

 

*al.* is presented in Sec. III. We provide details of a simplified *ab initio* computation which suggests that the parameters we used for fitting the experimental results are reasonable and characteristic of the Ar-W and Ar-*H*-W interaction potentials. The paper ends with a discussion in Sec. IV.

## II. THEORY OF RAINBOW SCATTERING

### A. The model

In this section we briefly review the results derived in Ref. 31. The potential of interaction $V(x,z)$ (with $x$, $z$ being the horizontal and vertical coordinates, respectively) of the incident particle whose mass is $M$ has two components. $\bar{V}(z)$ is the potential of interaction in the vertical direction (the distance between the incident atom and the surface). The corrugation potential has two Fourier components so that the full potential is modeled as

$$V(z,x) = \bar{V}(z) + \bar{V}'(z)\left[h_1 \sin\left(\frac{2\pi x}{l}\right) + h_2 \sin\left(\frac{4\pi x}{l}\right)\right]. \tag{2.1}$$

$h_1$ and $h_2$ are the respective corrugation heights for the first- and second-order Fourier terms and the prime denotes differentiation with respect to the argument.

Assuming small fluctuations due to the surface phonons and modeling them in terms of harmonic baths, we have that the Hamiltonian is

$$H = \frac{p_x^2 + p_z^2}{2M} + V(z,x) + \frac{1}{2}\sum_{j=1}^{N}\left[p_{j_z}^2 + \omega_{j_z}^2\left(x_{j_z} - \frac{c_{j_z}\sqrt{M}}{\omega_{j_z}^2}\bar{V}'(z)\right)^2\right] + \frac{1}{2}\sum_{j=1}^{N}\left[p_{j_x}^2 + \omega_{j_x}^2\left(x_{j_x} - \frac{c_{j_x}\sqrt{M}}{\omega_{j_x}^2}\frac{l}{2\pi}\sin\left(\frac{2\pi x}{l}\right)g(z)\right)^2\right], \tag{2.2}$$

where the horizontal and vertical bath degrees of freedom are characterized by the mass weighted momenta and coordinates $p_{j_i}$, $x_{j_i}$, $j=1,\ldots,N$; $i=x,z$. Translational invariance of the model is assured since the term coupling the horizontal motion to the respective phonon bath is periodic in the horizontal coordinate. The function $g(z)$ vanishes at large vertical distance so that when the particle is far from the surface it does not interact with it. The bath Hamiltonian (in mass weighted coordinates and momenta) is defined to be

$$H_B = \frac{1}{2}\sum_{j=1,\ i=x,z}^{N}(p_{j_i}^2 + \omega_{j_i}^2 x_{j_i}^2). \tag{2.3}$$

In the continuum limit the bath modes are described in terms of the spectral densities

$$J_i(\omega) = \frac{\pi}{2}\sum_{j=1}^{N}\frac{c_{j_i}^2}{\omega_{j_i}}\delta(\omega - \omega_{j_i}), \quad i = x,z \tag{2.4}$$

and associated friction functions

$$\eta_i(t) = \frac{2}{\pi}\int_0^\infty d\omega \frac{J_i(\omega)}{\omega}\cos(\omega t), \quad i = x,z. \tag{2.5}$$

We assume throughout that the friction functions are Ohmic, that is

$$\eta_i(t) = 2\eta_i\delta(t), \quad i = x,z. \tag{2.6}$$

### B. The angular distribution

The formal (classical limit) expression for the angular distribution in the Wigner representation takes the form

$$P(\theta) = \lim_{t\to\infty}\int_{-\infty}^{\infty}\prod_{j=1,\ i=x,z}^{N}\frac{dp_{j_i}dx_{j_i}}{2\pi\hbar}\int_{-\infty}^{\infty}dp_x dp_z dx dz \rho_{B,W}(\mathbf{p},\mathbf{x}) \times \rho_S(p_x,p_z,x,z)\delta\left[\theta - \tan^{-1}\left(\frac{p_x(t)}{p_z(t)}\right)\right] \tag{2.7}$$

where the notation $p_z(t)$, $p_x(t)$ stands for the classical time evolution. Here $\rho_S(p_x,p_z,x,z)$ is the Wigner representation of the incident wave packet and $\rho_{B,W}(\mathbf{p},\mathbf{x})$ is the Wigner representation of the thermal bath density, taken in the classical limit.

The incident particle at the time $-t_0$ is assumed to be defined by an incident Gaussian wavepacket $|\Psi\rangle$ centered about the incident momenta $p_{x0}$ and $p_{z0}$ and the coordinates $x_0$ and $z_0$. The incident energy is thus

$$E_0 = \frac{p_{x0}^2 + p_{z0}^2}{2M}. \tag{2.8}$$

The initial vertical momentum is taken to be negative, that is $p_{z0} \leq 0$. The incident scattering angle is by definition

$$\theta_0 = \tan^{-1}\left(\frac{p_{x0}}{p_{z0}}\right). \tag{2.9}$$

We will assume that the spatial width of the incident Gaussian wavepacket is sufficiently large that one can replace the Gaussian terms for the particle momenta with Dirac delta functions, that is the initial momenta have the unique values $p_{x0}$ and $p_{z0}$. One can then also integrate over the vertical coordinate, so that

$$P(\theta) = \frac{1}{l}\int_0^l dx \lim_{t\to\infty}\int_{-\infty}^{\infty}\prod_{j=1,\ i=x,z}^{N}\frac{dp_{j_i}dx_{j_i}}{2\pi\hbar}\rho_{B,W}(\mathbf{p},\mathbf{x}) \times \delta\left[\theta - \tan^{-1}\left(\frac{p_x(t_0)}{p_z(t_0)}\right)\right]. \tag{2.10}$$

The horizontal coordinate is defined as the impact parameter, so that the angular distribution is an average of an impact parameter-dependent angular distribution. The argument of the Dirac delta function is the (phonon-dependent) deflection function.

The final particle momenta are obtained by using classical perturbation theory in which the zeroth-order motion is that of the particle moving in the absence of coupling to the phonon bath and vanishing corrugation. It is then a matter of some algebra to find the explicit expression for the angular

distribution: the integration over the bath variables is effected as in Appendix A of Ref. 30. One finds that the angular distribution is given by the expression

$$P(\theta) = \frac{1}{l}\int_0^l dx \frac{1}{\sqrt{\pi\Sigma^2(x)}} \exp\left(-\frac{(\theta - \theta_d(p_{x0},p_{z0},x,\eta_x,\eta_z))^2}{\Sigma^2(x)}\right). \tag{2.11}$$

where the deflection function is

$$\theta_d(p_{x0},p_{z0},x,\eta_x,\eta_z) = -\theta_0 - K_1(p_{x0},p_{z0})\sin\left(\frac{2\pi}{l}x\right) - K_2(p_{x0},p_{z0})\sin\left(\frac{4\pi}{l}x\right) - \Delta\theta_1(x); \tag{2.12}$$

the rainbow angle functions are found to be

$$K_1(p_{x0},p_{z0}) = \frac{2\pi}{lp_{z0}}h_1\int_{-t_0}^{t_0} dt\bar{V}'(z_t)\cos(\omega_x t) \tag{2.13}$$

$$K_2(p_{x0},p_{z0}) = \frac{4\pi}{lp_{z0}}h_2\int_{-t_0}^{t_0} dt\bar{V}'(z_t)\cos(2\omega_x t); \tag{2.14}$$

and the horizontal frequency is defined as

$$\omega_x = \frac{2\pi}{l}\frac{p_{x0}}{M}. \tag{2.15}$$

The friction induced angular shift of the deflection function is given in terms of the energy losses to the bath and the function $g(z)$ coupling the vertical motion to the phonon motion

$$\Delta\theta_1(x) = \tan(\theta_{i0})\left(\frac{\langle\Delta E_B\rangle}{2E_0} - \frac{\eta_x}{2}\int_{-t_0}^{t_0} dtg^2(z_t)\right). \tag{2.16}$$

The average energy losses due to the vertical and horizontal motions are temperature independent and given by the expression (note that the dimension of $\eta_x$ is time$^{-1}$ while that of $\eta_z$ is time$^3$/mass$^2$)

$$\langle\Delta E_B\rangle_z = M\eta_z\int_{-t_0}^{t_0} dt\left(\frac{d\bar{V}'(z_t)}{dt}\right)^2 \tag{2.17}$$

for the vertical direction and

$$\langle\Delta E_B\rangle_x = \Delta\epsilon - \cos\left(\frac{4\pi x}{l}\right)\Delta\epsilon_x, \tag{2.18}$$

where

$$\Delta\epsilon = E_0\sin^2(\theta_{i0})\eta_x\int_{-t_0}^{t_0} dt\left[g^2(z_t) + \frac{1}{\omega_x^2}\left(\frac{dg(z_t)}{dt}\right)^2\right] \tag{2.19}$$

and

$$\Delta\epsilon_x = E_0\sin^2(\theta_{i0})\eta_x\int_{-t_0}^{t_0} dt\cos(2\omega_x t)\left[g^2(z_t) + \frac{1}{\omega_x^2}\left(\frac{dg(z_t)}{dt}\right)^2\right] \tag{2.20}$$

for the horizontal mode. It is of interest to note that the horizontal energy loss to the phonons depends on the impact parameter through the second-order Fourier term. The phonon interaction may thus lead to a phonon induced asymmetry in the angular distribution. The impact parameter-dependent variance of the angular distribution is

$$\Sigma^2(x) = \frac{\tan^2(\theta_{i0})}{\beta E_0}\left(\frac{\langle\Delta E_B\rangle}{E_0} + \eta_x\int_{-t_0}^{t_0} dtg^2(z_t)\times\left[1 - 2\cos\left(\frac{4\pi}{l}x\right)\right]\right) + \frac{\eta_x}{\beta E_0}\left(\int_{-t_0}^{t_0} dtg^2(z_t)\left[1 + \frac{\cos\left(\frac{4\pi}{l}x\right)\cos(2\omega_x t)}{\cos^2(\theta_{i0})}\right]\right). \tag{2.21}$$

### C. The angle-dependent energy loss

As shown in Ref. 30 one can use the same theory to obtain an explicit expression for the joint final angle and energy distribution. From this, one may derive an expression for the final average energy at a given final scattering angle. One finds

$$\langle E(\theta)\rangle = (E_0 - \langle\langle\Delta E_B\rangle\rangle_l) + \frac{2}{\beta P(\theta)}\frac{\partial}{\partial\theta}\langle P(\theta,x)\Delta\theta_1(x)\rangle_l \tag{2.22}$$

where $P(\theta,x)$ is the final angular distribution at a given impact parameter [it is the integrand of Eq. (2.11)] and the brackets denote averaging over the horizontal coordinate

$$\langle f\rangle_l = \frac{1}{lP(\theta)}\int_0^l dxf(x)P(\theta,x). \tag{2.23}$$

It is instructive to note that the angular dependence of the energy loss comes from the phonon induced shift of the deflection function $\Delta\theta_1(x)$. Roughly, if the shift is negative, then the contribution is positive and vice versa. Furthermore, if the dependence of the angular distribution on the impact parameter is weak, then at the peak of the angular distribution, the final average energy is just identical to the difference between the incident energy and the energy lost to the surface.

### D. Morse oscillator model

As shown in Ref. 31 the theory given in the previous section can be solved to a certain extent analytically when one chooses the vertical potential to be the Morse oscillator potential

$$\bar{V}(z) = V_0[1 - \exp(-\alpha z)]^2 - V_0. \tag{2.24}$$

where $V_0$ is the well depth and $\alpha$ is the Morse stiffness parameter. It is useful to define an energy-dependent frequency associated with the Morse oscillator

$$\Omega^2 = \frac{2\alpha^2 E_z}{M} = \frac{\alpha^2 p_z^2}{M^2}; \tag{2.25}$$

an energy-dependent angular variable

$$\cos(\Phi) = -\sqrt{\frac{V_0}{(E_z + V_0)}}, \quad \sin(\Phi) = \sqrt{\frac{E_z}{(E_z + V_0)}}, \tag{2.26}$$

and the reduced frequency

$$\bar{\Omega} = \frac{\omega_x}{\Omega} = \frac{2\pi}{\alpha l}|\tan(\theta_{i0})|. \tag{2.27}$$

One then finds that the analytical expressions for the rainbow angle functions are

$$K_1(E_0, \theta_{i0}) = \frac{4\pi^2 h_1 \bar{\Omega}\cosh(\bar{\Omega}\Phi)}{l\sinh(\bar{\Omega}\pi)} \tag{2.28}$$

$$K_2(E_0, \theta_{i0}) = \frac{16\pi^2 h_2 \bar{\Omega}\cosh(2\bar{\Omega}\Phi)}{l\sinh(2\bar{\Omega}\pi)}. \tag{2.29}$$

Since the angle $\Phi$ ranges from $\pi$ to $\pi/2$ as the vertical energy increases from 0 to $\infty$ one sees (provided that the reduced frequency $\bar{\Omega}$ is on the order of unity or larger) that the rainbow angle functions decrease monotonically as the energy increases. Furthermore, the ratio of the second-order rainbow function to the first-order rainbow function

$$\frac{K_2(p_0, \theta_{i0})}{K_1(p_0, \theta_{i0})} = \frac{2h_2\cosh(2\bar{\Omega}\Phi)}{\cosh(\bar{\Omega}\pi)h_1\cosh(\bar{\Omega}\Phi)} \tag{2.30}$$

also decreases as a function of energy. This implies that typically the asymmetry induced by the second-order term will be smaller as the energy increases and is a key to understanding some of the experimental results found for the scattering of Ar on the hydrogen covered tungsten surface.

The energy loss in the vertical direction is then found to be

$$\langle \Delta E_B \rangle_z = \frac{4M\eta_z\Omega\alpha^2 V_0^2}{15}\left(\frac{(\cos^4(\Phi) + 28\cos^2(\Phi) + 16) - 15\Phi\cot(\Phi)[2 + \cos^2(\Phi)]}{\cos^4(\Phi)}\right) \tag{2.31}$$

Specifying the function $g(z)$ which couples the phonons to the horizontal motion to be

$$g(z) = \exp(-2\alpha z). \tag{2.32}$$

one finds

$$\frac{1}{2}\int_{-t_0}^{t_0} dt g^2(z_t) = \frac{\sin^2(\Phi)}{\Omega}\left(\frac{11\cos^2(\Phi) + 4 - 3\Phi\cot(\Phi)[2\cos^2(\Phi) + 3]}{6\cos^4(\Phi)}\right) \tag{2.33}$$

$$\Omega\int_{-\infty}^{\infty} dt g^2(z_t)\cos(2\omega_x t) = \frac{2\pi\sin^2(\Phi)\sinh(2\bar{\Omega}\Phi)}{3\cos^4(\Phi)\sinh(2\bar{\Omega}\pi)} \times\left[\coth(2\bar{\Omega}\Phi)\{4\bar{\Omega}^3\sin^2(\Phi) + \bar{\Omega}[11\cos^2(\Phi) + 4]\} - 6\bar{\Omega}^2\sin(2\Phi) - \cot(\Phi)\left(3\cos^2(\Phi) + \frac{9}{2}\right)\right] \tag{2.34}$$

$$\Delta\epsilon = \frac{M\bar{\Omega}^2\eta_x\Omega l^2}{24\pi^2}\sin^2(\Phi)\left(\frac{11\cos^2(\Phi) + 4 - 3\Phi\cot(\Phi)[2\cos^2(\Phi) + 3]}{\cos^4(\Phi)}\right) + \frac{M\eta_x\Omega l^2}{120\pi^2}\left(\frac{6\cos^4(\Phi) + 83\cos^2(\Phi) + 16 - 15\Phi\cot(\Phi)[4\cos^2(\Phi) + 3]}{\cos^4(\Phi)}\right) \tag{2.35}$$

$$\Delta\epsilon_x = \frac{M\eta_x\Omega l^2}{60\pi\cos^4(\Phi)\sinh(2\bar{\Omega}\pi)}\cosh(2\bar{\Omega}\Phi)\cdot(4\bar{\Omega}^5\sin^4(\Phi) + \bar{\Omega}^3\sin^2(\Phi)[35\cos^2(\Phi) + 20] + \bar{\Omega}[6\cos^4(\Phi) + 83\cos^2(\Phi) + 16]) - \frac{M\eta_x\Omega l^2}{24\pi\cos^3(\Phi)\sinh(2\bar{\Omega}\pi)}\sinh(2\bar{\Omega}\Phi)\cdot\left(8\bar{\Omega}^4\sin^3(\Phi) + \bar{\Omega}^2\sin(\Phi)[10\cos^2(\Phi) + 29] + 3\frac{4\cos^2(\Phi) + 3}{\sin(\Phi)}\right) \tag{2.36}$$

and this is all that is needed to compute the angular shift of Eq. (2.16); the variance as given in Eq. (2.21); and thus the angular distribution as given in Eq. (2.11). The remaining integration over the horizontal coordinate needs to be carried out numerically.

## III. THEORY OF Ar-2*H*-W(100) SCATTERING

### A. Experimental fits

There are six free parameters in the corrugated Morse oscillator model—the well depth of the Morse oscillator $V_0$; the Morse oscillator stiffness parameter $\alpha$; the corrugation parameters $h_1$ and $h_2$ and the Ohmic friction coefficients $\eta_x$ and $\eta_z$. The lattice length $l=4.6$ Å is known[10] and the mass of Ar is $M=39$ amu. One may be cynical and claim that almost anything can be fit with a six parameter theory, however we will show how the extensive experimental results do not give much leeway in determining them.

Our starting point is Fig. 8 of Ref. 10. One observes an asymmetry in the angular distributions, but it is not very strong. This implies that the second-order corrugation height will be small as compared with the first-order corrugation height—$h_2/h_1 \ll 1$. To zeroth order then one should consider the incident energy and angle dependence of the first-order rainbow function $K_1$. From the figure, one also observes that at the angle of incidence of $-30°$ and a surface temperature of $T=90$ K, the distance between the rainbow angles decreases from a value of $\sim 23°$ at $E_0=65$ meV to $\sim 11°$ at $E=220$ meV. This implies that the rainbow angle function $K_1$ [see Eq. (2.28)] must be a decreasing function of the energy. As noted in the previous section, this in turn implies that the reduced frequency $\bar{\Omega} \geq 1$. At the same time, the decay of the rainbow function increases exponentially with the magnitude of the reduced frequency. Therefore, the reduced frequency cannot be too large. There is though a third piece of information. From Fig. 14 of Schweizer *et al.* we know that at the 60° angle of incidence, the rainbow structure disappears, implying that the value of the rainbow function $K_1$ at this angle must be smaller than its value at 30°. Since the magnitude of $\bar{\Omega}$ is determined by the product $\alpha l$ ($\alpha$ is the Morse potential stiffness parameter) these observations lead to the conclusion that the product $\alpha l \simeq 2$. With some fine tuning we then determined that $\alpha l=2$ is optimal and used this throughout.

The same information helps in determining the Morse potential well depth $V_0$. As mentioned, the experiment shows that the rainbow function decreases rather quickly with energy. This implies that the angle $\Phi$ must change rather rapidly with energy, as it is $\Phi$ which determines the energy dependence of the rainbow function. The well depth must thus be of the same order of magnitude as the energy at which the rainbow function changes rapidly, which in turn sets the value of $V_0 \simeq 50$ meV. In practice, we found that our "best" fit of the data was obtained using $V_0=60$ meV, and this is the value used throughout this paper. (This is somewhat smaller then the value of 100 meV employed by Schweizer *et al.*). In addition, the actual measured magnitude of the distance between the rainbow peaks sets the magnitude of the primary corrugation parameter as $h_1 \simeq 0.1$ a.u., which is approximately double the corrugation height used by Schweizer *et al.* in their analysis. In practice we employed the value $h_1=0.099$ a.u.

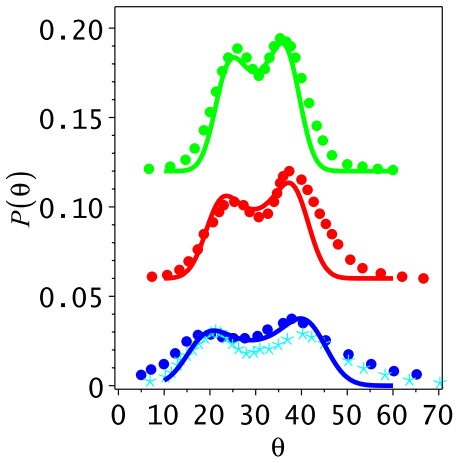


FIG. 1. (Color online) Energy dependence of the angular distributions for a $-30°$ angle of incidence and $T=90$ K. The solid circles and asterisks are the experimental results adapted from Figs. 8 and 12 of Ref. 10. The plots from bottom to top are for the incidence energies of 65, 130, and 220 meV, respectively, and have been shifted by 0.06 for the sake of clarity. From bottom to top, the normalized theoretical distributions have been multiplied by the constant factors of 1, 1.1, and 1.25 so as to compare with the (unnormalized) experimental results.

We are thus left with the fitting of three parameters, the friction coefficients and the second-order corrugation height $h_2$. From Fig. 12 of Ref. 10 we note that the experimentally measured average energy lost to the surface is $\sim 7$ meV at the $-30°$ angle of incidence and surface temperature $T=90$ K. This sets the limits for the sum of the two friction coefficients. Their ratio is obtained by noting that under all conditions, the center of the measured angular distribution is approximately specular. This implies that the friction induced shift function $\Delta\theta_1$ [see Eq. (2.16)] must be small at all incidence energies. This then led to the reduced values of the friction coefficients $\eta_x/\omega_0=.00267$ (where $\omega_0=\alpha\sqrt{(2V_0/M)}$ is the harmonic frequency of the Morse potential) and $M^2\omega_0^3\eta_z=0.00228$. The second-order corrugation parameter, is responsible for the asymmetry of the angular distribution.[31] It may thus determined by the asymmetry of the measured angular distribution at the 30° angle of incidence. Our optimized value was $h_2=-0.007$ a.u. which we note is indeed much smaller than the first-order corrugation height.

Results for the angular distribution for $\theta_0=-30°$ and the different incidence energies are presented in Fig. 1. The solid circles are the experimental results adapted from Fig. 8 of Ref. 10, the solid lines are the theoretical fits as obtained with the parameter set described above. The incident energies are from bottom to top 65, 130, and 220 meV, respectively (the distributions are displaced by 0.06 for the sake of clarity). Note that for the 65 meV case we plot on the figure two different experimental distributions, the asterisks are adapted from the bottom half of Fig. 12 of Ref. 10. The two

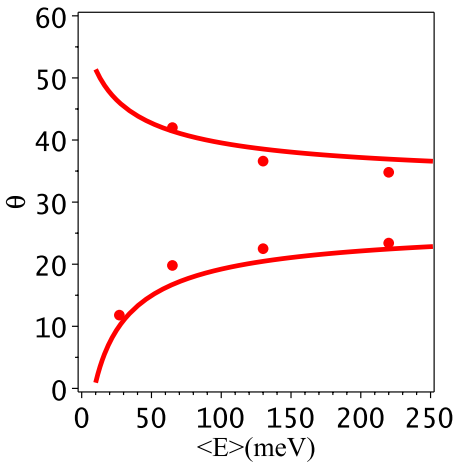


FIG. 2. (Color online) Incident energy dependence of the rainbow angles. The solid lines are the theoretical estimates, the solid circles are the experimental results adapted from Fig. 11 of Ref. 10.

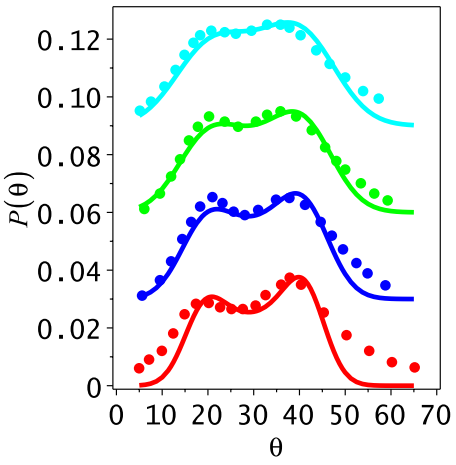


FIG. 3. (Color online) Temperature dependence of the angular distributions for a −30° angle of incidence and 65 meV incidence energy. The solid circles are the experimental results adapted from Fig. 10 of Ref. 10. The plots from bottom to top are for the surface temperatures of 90, 140, 190, and 250 K, respectively, and have been shifted by 0.03 for the sake of clarity. From bottom to top, the normalized theoretical distributions have been multiplied by the constant factors of 1, 1.1, 1.14, and 1.25 so as to compare with the (unnormalized) experimental results.

experimental distributions are not identical, the one from Fig. 8 has a larger rainbow peak for subspecular angles, while the distribution of Fig. 12 has the larger rainbow peak at superspecular angles. We believe that this provides a rough indication of the experimental error in the angular distributions. In all of our fits the differences between them and the experimental results are not substantially larger than the differences between the two experimental distributions, implying that given the published data and their uncertainty, our fits are satisfactory.

Schweizer *et al.* also measured the angular distribution for $E_0$=27 meV. This is very low energy, where on the one hand quantum diffraction effects are noticeable in the experimental results and on the other hand at such low energies, the perturbation theory we are using is no longer very accurate. We have therefore omitted results for this low energy, even though qualitatively our theory is reasonable.

As already discussed, the distance between the rainbow angles decreases with decreasing energy. From Ref. 31 we note that in the presence of weak asymmetry, the rainbow angles are given by $\pm K_1+K_2$. These two values are plotted as a function of the energy in Fig. 2 and compared with the experimental values adapted from Fig. 11 of Schweizer *et al.* One notices the good agreement. In this figure we added also the lower rainbow angle for the low incidence energy of 27 meV.

Schweizer *et al.* also reported in their Fig. 10 the surface temperature dependence of the angular distributions measured at $\theta_0$=−30°, $E_0$=65 meV and $T$=90, 140, 190, and 250 K. The theory is compared with the experimental results in Fig. 3. The central feature of the four distributions (displaced from each other by 0.03) is that the rainbow peaks are broadened as the temperature is increased. This is predicted from our theory since the variance of the distribution ($\Sigma^2$) increases linearly with the temperature. This broadening smears out the rainbows and their asymmetry, the rainbow peaks become less significant as the temperature is increased.

Perhaps the most puzzling aspect of the Ar-2*H*-W(100) system was the drastic change in the angular distribution with the angle of incidence. As shown in Fig. 14 of Ref. 10 when the angle of incidence is increased to −60° the rainbow feature seems to disappear. One is left with a rather broad bell shaped distribution which is quasispecular. As already indicated in the previous section the reason for this is that the rainbow angle functions decrease with increasing angle of incidence. This is shown in Fig. 4 where we plot the dependence of $K_1$ and $K_2$ on the angle of incidence at $E_0$=65 and 110 meV. At the higher energy, $K_1$ decreases from a value of 9.7° at $\theta_0$=−30° to 5.5° at $\theta_0$=−60°. Similarly, for $E_0$ =65 meV, $K_1$ decreases from a value of 12.4° at $\theta_0$=−30° to 9.7° at $\theta_0$=−60°. This decrease in the distance between the rainbow angles then leads to the unimodal peaks shown in

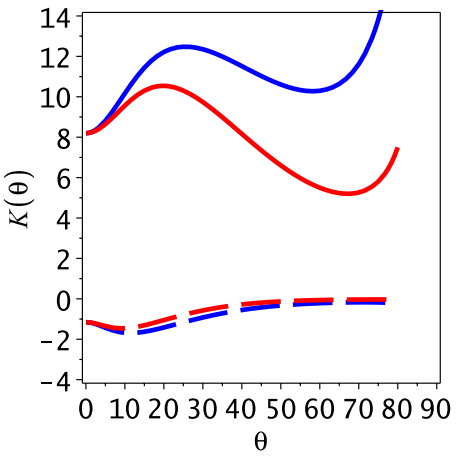


FIG. 4. (Color online) Incident angle dependence of the rainbow functions. The solid lines are for $K_1$, the dashed lines are for $K_2$. The upper solid line is for $E_0$=65 meV, the lower solid line is for $E_0$=110 meV. Likewise the upper dashed line is for $E_0$ =110 meV, while the lower dashed line is for $E_0$=65 meV. For further details see the text.

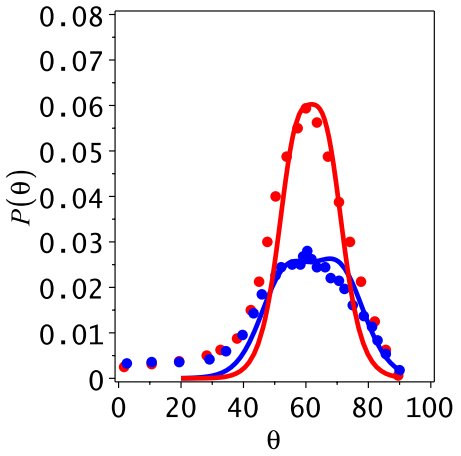


FIG. 5. (Color online) Energy dependence of the angular distributions for a −60° angle of incidence and $T=90$ K. The solid circles are the experimental results adapted from Fig. 14 of Ref. 10. The plots are for the incidence energies of 65 and 110 meV, the broader plot is at the lower energy. The normalized theoretical distributions at $E_0=65$ and 110 meV have been multiplied by the respective constant factors of 0.93 and 1.35 so as to compare with the (unnormalized) experimental results.

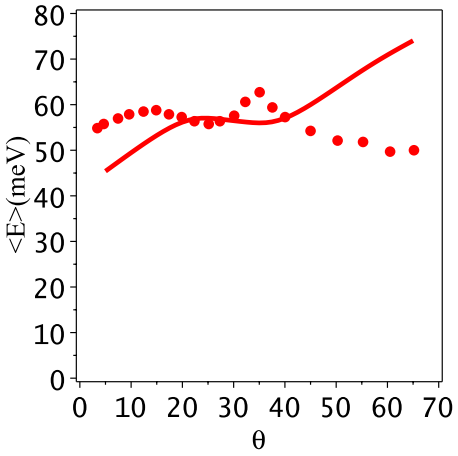


FIG. 6. (Color online) Final angle dependence of the final average energy for the −30° angle of incidence and $T=90°$. The solid circles are the experimental results adapted from Fig. 12 of Ref. 10. The solid line is the theoretical result as obtained from Eq. (2.22). For further details see the text.

Fig. 5 and compared with the experimental distributions. Note especially that when $E_0=65$ meV, the theoretical angular distribution is quite flat about the maximum, the width is due to the two rainbow angles which are smeared due to the coupling to the phonons. In fact, if one would lower the temperature, we predict that the angular distribution even at this large angle of incidence would again become bimodal, reflecting the rainbow scattering. The theoretical full widths at half maximum of the theoretical angular distributions shown in the figure are 34° and 21° for the low and high energies, respectively, these should be compared with the respective experimental values of 36° ± 3° and 25° ± 2° as reported in Fig. 15 of Schweizer *et al.*

We also note from Fig. 4 that the absolute magnitude of $K_2$ decreases with increasing angle of incidence, faster than $K_1$. For $\theta_0=-30°$ $K_2=0.9°$ for $E_0=65$ meV and 0.6° for $E_0=110$ meV. However, when the angle of incidence is $\theta_0=-60°$ the respective values of $K_2$ are 0.2° and 0.06°. It is thus not surprising that the asymmetry almost disappears at the larger angle of incidence.

The last challenge presented by the experimental data is the final angular dependence of the measured energy loss. Comparison between experiment and theory is shown in Fig. 6. The agreement here is qualitative. The two lines coincide more or less around the maximal region of the angular distribution where they also do not change much with the final angle, however the theory does not account well for the details of the experimental measurement. Theoretically, far away from the maximum of the distribution the theoretical form is Gaussian. The logarithmic derivative of the Gaussian is linear, therefore for small and large angles one notes a linear increase in the average final energy with increasing final angle. This linearity is not found in the experimental data. The overall average energy loss is though well reproduced by the theory.

### B. Quantum chemical methods

#### *1. Computational methodology*

To ascertain whether the fitted model parameters are sensible it is also of value to gain independent estimates of the well depth and stiffness parameter of the vertical potential. For this purpose we undertook *ab initio* computations of the potential energy between an Ar atom and a hydrogen atom bound collinearly to a tungsten atom and the same for the interaction of an Ar atom with an isolated tungsten atom. The accurate calculation of these potentials is not a routine task because correlated methods with large basis sets are mandatory for a reliable account of the van der Waals interaction. As an additional challenge, the rather high nuclear charge of the tungsten atom ($Z=74$) calls for a relativistic description. For meeting these requirements we pursued two different routes, described below.

(1) As an effective and cost saving but still accurate means to compute potential energy curves, we employed the approximate coupled cluster doubles model RICC2[32–34] from the TURBOMOLE program package.[35] For hydrogen and argon, augmented correlation consistent basis sets with quintuple zeta quality and polarization functions (aug-ccpV5Z)[36,37] were used. For the tungsten atom, the Stuttgart relativistic energy consistent effective core potential[38] (ECP) with 14 valence electrons (5*s*, 5*p*, 5*d*, and 6*s*) was employed. A corresponding quadruple zeta basis set with two sets of polarization functions (termed ecp-60-mwb-QZVPP,[39]) from the TURBOMOLE basis set library was used for the valence shells of the tungsten atom. Test calculations with more expensive tungsten valence basis sets from the TURBOMOLE library, in particular the ecp-60-mwb-QZV5f4g3h set, showed that the results from the ecp-60-mwb-QZVPP basis set are essentially converged.

Molecular spin orbitals (MSOs) were obtained from unrestricted Hartree-Fock (UHF) theory. For all species under investigation, symmetry restrictions from the $C_{2v}$ point group were imposed. For the W···Ar system, we chose two differ-

ent sets of MSO occupations: the first one ($\alpha$ MSOs: $1-10a_1$, $1-4b_1$, and $1-4b_2$; $\beta$ MSOs: $1-8a_1$, $1-3b_1$, and $1-3b_2$) formally corresponds to a tungsten atom with either $6s^25d^4$ configuration with a $^5D$ term symbol or to a $6s^15d^5$ configuration with a $^5D$ or a $^5G$ term symbol. According to Hund's rules and assuming a $6s^25d^4$ ground state configuration for tungsten,[40] the $^5D$ term is supposed to be the lowest one. The second occupation ($\alpha$ MSOs: $1-10a_1$, $1a_2$, $1-4b_1$, and $1-4b_2$; $\beta$ MSOs: $1-7a_1$, $1-3b_1$, and $1-3b_2$) represents the nearly degenerate $^7S$ term of tungsten which originates from a $6s^15d^5$ configuration with a half-filled $5d$ shell. In the case of the (W-H)$\cdots$Ar system, an occupation $1-10a_1$, $1a_2$, $1-4b_1$, $1-4b_2$ ($\alpha$ MSOs), and $1-8a_1$, $1-3b_1$, $1-3b_2$ ($\beta$ MSOs) is chosen in accord with a $X\ ^6\Sigma^+$ ground state for the W-H molecule. Such a ground state has been revealed by correlated relativistic all-electron calculations.[41]

Auxiliary basis sets[42,43] for the computation of the two-electron integrals via the resolution-of-the-identity (RI) approach in the RICC2 calculations were taken from the TURBOMOLE basis set library. Throughout, the $1s$, $2s$, and $2p$ electrons of argon were treated as a frozen core in the RICC2 runs.

(2) To ensure that correlation of the tungsten core (in particular the $4f$ electrons) does not have a drastic impact on the dispersion energy, all-electron calculations were carried out with the MOLPRO program package.[44] The atomic natural orbital relativistic correlation-consistent (ANO-RCC) basis set of Roos *et al.*[45] was used for the tungsten atom. Second-order Douglas-Kroll-Hess kinematic relativistic corrections[46,47] to the one-electron integrals were included. The final correlation treatment was done at the level of coupled cluster singles doubles with perturbative triples correction [CCSD(T)].[48] The one-particle basis sets were comprised either by (relativistic) HF molecular orbitals (MOs) with open-shell occupations in accord with the unrestricted HF occupations described above or pseudocanonical MOs from the multiconfiguration self-consistent field program MULTI.[49,50] The pseudocanonical orbitals resulted from complete active space self-consistent field (CASSCF) calculations with active spaces as follows: for the Ar/W potential, we performed (6,10)-CASSCF calculations with 6 electrons in 10 active orbitals. The active space was comprised by the $6s$, $5d$, and $6p$ orbitals of the tungsten atom (denoted $21-24a_1$, $4a_2$, $11-12b_1$, and $11-12b_2$ in the $C_{2v}$ point group). In the case of the Ar/($H$-W) system, one additional electron from the hydrogen led to a (7,10)-CASSCF. The active space consisted of the bonding orbital between hydrogen and tungsten denoted as $6s$(W)+$1s$(H), the $5d$, and the $6p$ orbitals of the tungsten atom (in the $C_{2v}$ point group with the same notation as above). In the CCSD(T) calculations these active orbitals and the tungsten $4f$ orbitals were correlated.

To arrive at interaction potentials which are approximately free from the well-known basis set superposition error, we carried out counter-poise corrections,[51] throughout. Within this scheme, the interaction potential is obtained as the difference of the energy of the complete system and the energies of the fragments as calculated using the basis sets of the whole system

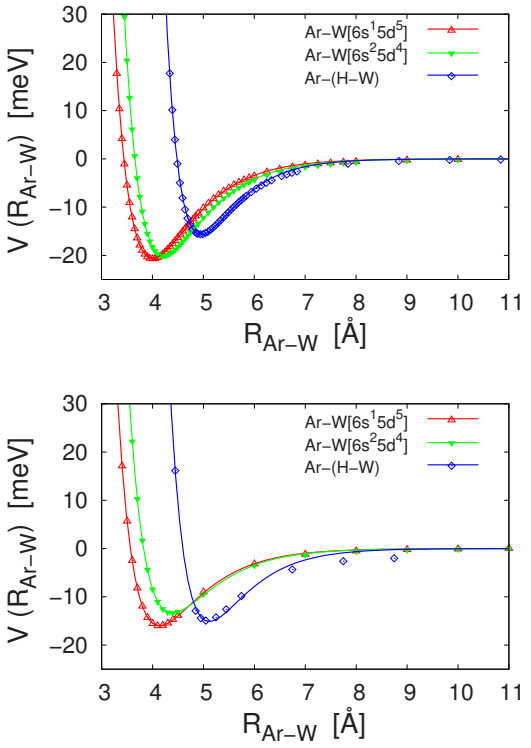


FIG. 7. (Color online) *Ab initio* interaction potentials for the model systems. Top panel: results from the UHF+RICC2 calculations with ECPs for the tungsten atom. Bottom panel: relativistic all-electron calculations at the CASSCF+CCSDT(T) level of theory. The graphs display the calculated *ab initio* data together with the fitted Morse potential energy curves whose parameters are given in Table I.

$$V^{(CPC)}[A-B](R) = E_{A,B}[A-B](R) - E_{A,B}[A](R) - E_{A,B}[B](R). \tag{3.1}$$

The *ab initio* data were finally fitted to the Morse potential energy functions [Eq. (2.24)]. Harmonic vibrational frequencies at the equilibrium geometries were obtained from the potential parameters and the reduced mass $\mu$ according to

$$\omega_e = \alpha\sqrt{\frac{2D_e}{\mu}}. \tag{3.2}$$

In the case of the (W-H)$\cdots$Ar complex, we optimized the geometry of the complex at the RICC2 level. For the all-electron calculations on (W-H)$\cdots$Ar the bond length of the W-H molecule was optimized at the CASSCF level. The potential energy curves were generated by varying the H-Ar distance, but keeping the W-H bond length fixed at the respective optimum value.

### 2. Results of the ab initio computations

The interaction potentials from the *ab initio* calculations are shown in Fig. 7. The corresponding parameter sets for the fitted Morse potential functions are compiled in Table I. The AE/HF+CCSDT(T) calculations are not shown in Fig. 7 and Table I. They yielded essentially the same result as the AE/CASSCF+CCSDT(T) calculations for (W-H)$\cdots$Ar and

TABLE I. Calculated and fitted Morse potential parameters.

| System | State/term | Method | $D_e$ (meV) | $\alpha$ (Å$^{-1}$) | $R_e$ (Å) | $\omega$ (cm$^{-1}$) |
|---|---|---|---|---|---|---|
| Ar-W | W: $^7S$ $[6s^15d^5]$ | ECP/UHF+RICC2 | 20.6 | 1.23 | 4.00 | 22.6 |
| Ar-W | W: $^5D$ $[6s^25d^4]$ | ECP/UHF+RICC2 | 20.0 | 1.23 | 4.22 | 22.5 |
| Ar-(H-W) | $X\ ^6\Sigma^+$ | ECP/UHF+RICC2 | 15.7 | 1.44 | 4.96 | 23.3 |
| Ar-W | W: $^7S$ $[6s^15d^5]$ | AE/CAS+CCSD(T) | 16.0 | 1.21 | 4.13 | 19.8 |
| Ar-W | W: $^5D$ $[6s^25d^4]$ | AE/CAS+CCSD(T) | 13.4 | 1.23 | 4.39 | 18.3 |
| Ar-(H-W) | $X\ ^6\Sigma^+$ | AE/CAS+CCSD(T) | 15.1 | 1.33 | 5.11 | 21.1 |
| fit | | | 60.0 | 0.43 | | 13.7 |

Ar-W with tungsten in the $^7S$ $[6s^15d^5]$ state, but were hampered by severe convergence problems in the HF runs for the $^5D$ $[6s^25d^4]$ state.

The computations reveal that the van der Waals interaction between an argon atom and a tungsten atom or a tungsten hydride molecule is rather weak: throughout, we obtain binding energies $D_e$ around 20 meV or less. Not surprisingly, the dispersion interaction between an Ar atom and an isolated, extended W atom is somewhat stronger than the interaction for an Ar atom approaching a H-W molecule with the compact, unpolarizable H atom being in the middle. The equilibrium distance between the argon and the tungsten atoms is of course increased at the same time (from ~4 to ~5 Å). Noteworthy, though, the difference between the binding energies $D_e$ of W$\cdots$Ar and (W-H)$\cdots$Ar is to a large extent leveled out in the AE/CASSCF+CCSD(T) potentials. We did not systematically investigate why this happens. Employing our numerical results from the molecular calculations to the surface scattering problem, we may roughly estimate that the depth of the potential well for the hydrogen-covered tungsten surface is at least approximately 75% of the value for the bare metal surface.

Following, we add some remarks referring to the reliability and accuracy of our calculations. First, we note that in both our approaches the septet tungsten ($^7S$ term from the half-filled $6s^15d^5$ configuration) appears to be slightly more stable than the computed quintet state ($^5D$ term from the $6s^25d^4$ configuration). The energetic separation amounts to about 3200 cm$^{-1}$ at the ECP/UHF+RICC2 level and ~2400 cm$^{-1}$ in the AE/CASSCF+CCSD(T) approach. The same order of states was already found in ECP/HF calculations in Ref. 38. From experiment, the separation of the two terms is known to be on the order of the fine-structure splittings, e.g.: $E(^7S_{J=3})-E(^5D_{J=0})=2951$ cm$^{-1}$, but $E(^5D_{J=4})-E(^5D_{J=0})=6219$ cm$^{-1}$.[40] It is thus clear that we do not get the correct order of states without a proper account of spin-orbit coupling.

For the H-W molecule in the $X\ ^6\Sigma^+$ state, the optimized bond distance is $R_e=1.682$ Å within the ECP/UHF+RICC2 treatment. We also computed a harmonic vibrational frequency $\omega_e=1837$ cm$^{-1}$ analytically at the ECP/UHF level where the optimized bond length is $R_e=1.757$ Å. Corresponding experimental values are $R_e=1.79\pm0.02$ Å and $\omega_e=531\pm62$ cm$^{-1}$,[52] respectively. From the CASSCF computations, we obtained an optimized H-W bond length of $R_e=1.746$ Å. In Ref. 41, values $R_e=1.727$ Å and $\omega_e=1897$ cm$^{-1}$ were derived from correlated spin-free all-electron calculations. In addition, a critical discussion of the experimental vibrational frequency was given there. We conclude that our description of the electronic structure of the H-W molecule in the $X\ ^6\Sigma^+$ state is quite reasonable.

The spin contamination encountered in the UHF calculations remained within acceptable margins: at the UHF level, expectation values of the total electronic spin operator $\langle \mathcal{S}^2 \rangle$ differed from their theoretical pure spin values $S(S+1)$ by at most 0.052. Typical values for the coupled cluster diagnostics were $D_1 \approx 0.03-0.07$ in the RICC2 calculations, and $D_1 \approx 0.03-0.06$ and $T_1 \approx 0.003-0.01$ in the R-CCSDT(T) runs, respectively.

Overall, the results from the ECP and the all-electron calculations differ only by approximately 25 % for the bonding energy. Taking into account that this quantity is only a tiny fraction of the involved total electronic energies (e.g. $<5\times10^{-8}$ of the electronic energy of approximately $-16128.67E_H$ for the tungsten atom), such a degree of agreement between completely independent calculations is very good. At the same time, the correlation of the tungsten $4f$ electrons does not substantially alter the result.

Comparison of the quantum chemistry results given in Table I and the fitted parameters obtained from the Morse potential model for the scattering shows that the fitted well depth of 60 meV is somewhat too large (compared to the theoretical well depth of ~20 meV) and that the fitted frequency of 14 cm$^{-1}$ is a bit small (as compared with the theoretical frequency of ~20 cm$^{-1}$). In different terms, the fitted stiffness parameter seems too small, increasing the stiffness parameter would increase the frequency while decreasing the well depth decreases the frequency but only as the square root of the well depth. In this context we do note that the theory does not take into account that the approaching Ar atom interacts with more than one hydrogen and tungsten atom at a time. It could well be that a more complete quantum chemical computation would then lead to a larger well depth and smaller stiffness parameter. With this in mind, we believe that the present quantum chemistry computations suggest that the fitted parameters are in the correct "ball park."

## IV. DISCUSSION

The experimental results for in-plane scattering of Ar from a $2H$-W(100) surface, measured almost twenty years ago were shown to fit well to a corrugated Morse potential model and a perturbation theory approximation for the classical dynamics of the scattering event. The corrugation had to include the first two Fourier terms, the first term accounts for the overall rainbow features, the second order term is responsible for the asymmetry in the angular distributions. The corrugation heights $h_1$ and $h_2$ are independent of the initial energy. The corrugation itself is a feature of the force field and not the dynamics. The rainbow functions $K_1$ and $K_2$ are energy dependent, the higher the energy, the stronger is the impulse given in the vertical direction. This affects the rainbow functions and is responsible for the narrowing of the distance between the rainbows as energy is increased.

We have shown that the corrugated Morse potential model accounts well for the main experimental features: decrease in the distance of the rainbow angles with increasing scattering energy; increase in the width of the angular distribution with increasing surface temperature; change in the angular distribution from a bimodal distribution at low angle of incidence to a unimodal quasispecular angular distribution at high angle of incidence; energy dependence of the widths of the angular distribution and average energy loss to the surface. This analysis shows that there is really nothing very special about the Ar-$H$-W(100) data, in the sense that it may all be explained within the framework of a classical scattering theory.

The results presented here are a further affirmation of the strength of the classical perturbation theory and its usefulness for understanding heavy atom surface scattering. Although when applied to the Morse potential model, there are 6 free parameters, we have shown that a few experimental results allow for their systematic extraction. Comparison with simplified *ab initio* computations shows that the values used are realistic. The *ab initio* computations predict a well depth on the order of $\sim 20$ meV, which is smaller than the fitted value of 60 meV. We note though that in a more accurate computation, the Ar atom would "feel" the effect of more than one tungsten atom on the surface and this could lead to a sizable increase in the well depth. It is evident that one should undertake a more complete *ab initio* study of the Ar-$H$-W surface interaction potential.

In all of our papers thus far, the model has been used *a posteriori* but not predictively. The results shown in this paper do predict that if one would further lower the surface temperature one would measure the rainbow structure even when the angle of incidence is $-60°$. Furthermore, in its present form, we used a classical thermal distribution for the phonon modes. This leads to a linear dependence of the variance of the angular distribution on the temperature, as also seen in the present experiments. However, at very low temperature, this approximation will fail and one should see that the width becomes independent of the temperature. To the best of our knowledge, this qualitative quantum mechanical result has not been measured thus far for atom surface interaction.

The theory we have used is based on a Langevin equation description for the interaction of the incident atom with the phonons of the surface. This is an approximation, though perhaps a good one. Ultimately, the "correct" way to study atom-surface scattering is to employ on the fly classical dynamics.[53–56] The analysis of this paper, indicates that the classical approximation is not a problem, the major difficulty would be to obtain an accurate estimate of the force field between the atom and the surface. Given present computational power, such a program should be possible. This is important not only for atom surface scattering but also for molecular scattering from surfaces. It is much more difficult to provide for an analytic theory even for diatomic scattering, without making some drastic approximations. However, on the fly computations remain feasible.

Finally we note that the present analysis is incomplete as it is classical in nature. The experimental findings indicate quantum diffraction for the scattering of Ar on the $2H$-W(100) surface. These present a challenge to the present model in the context of quantum surface scattering computations.[57,58] If it is correct then the same potential energy surface used in the classical theory should account for the diffraction phenomena. In this context we note our recent semiclassical computations for the scattering of He from a corrugated surface.[59] It should be interesting to see whether the same semiclassical theory can also account for the diffraction of Ar scattering from surfaces.

## ACKNOWLEDGMENTS

We thank S. Miret-Artés for stimulating discussions. We gratefully acknowledge financial support of this work by the Israel Science Foundation and the Minerva Foundation. Computation time was provided by the Institute of Theoretical Chemistry, Heinrich Heine Univ. (Düsseldorf).

*eli.pollak@weizmann.ac.il

[1] A. W. Kleyn and T. C. M. Horn, Phys. Rep. **199**, 191 (1991).
[2] J. D. McClure, J. Chem. Phys. **51**, 1687 (1969).
[3] R. A. Oman, J. Chem. Phys. **48**, 3919 (1968).
[4] J. N. Smith, D. R. O'Keefe, and R. L. Palmer, J. Chem. Phys. **52**, 315 (1970).
[5] E. Hulpke, Surf. Sci. **52**, 615 (1975).
[6] K. H. Rieder and W. Stocker, Phys. Rev. B **31**, 3392 (1985).
[7] T. Engel and J. H. Weare, Surf. Sci. **164**, 403 (1985).
[8] A. Amirav, M. J. Cardillo, P. L. Trevor, C. Lim, and J. C. Tully, J. Chem. Phys. **87**, 1796 (1987).
[9] E. K. Schweizer and C. T. Rettner, Phys. Rev. Lett. **62**, 3085 (1989).
[10] E. K. Schweizer, C. T. Rettner, and S. Holloway, Surf. Sci. **249**, 335 (1991).
[11] B. Berenbak, S. Zboray, B. Riedmuller, D. C. Papageorgopoulos,

S. Stolte, and A. W. Kleyn, Phys. Chem. Chem. Phys. **4**, 68 (2002).
[12] T. Kondo, H. S. Kato, T. Yamada, S. Yamamoto, and M. Kawai, Eur. Phys. J. D **38**, 129 (2006).
[13] P. Jewsbury, Surf. Sci. **52**, 325 (1975).
[14] E. F. Greene and E. A. Mason, Surf. Sci. **75**, 549 (1978).
[15] J. R. Klein and M. W. Cole, Surf. Sci. **79**, 269 (1979); , **81**, L319 (1979).
[16] J. C. Tully, J. Chem. Phys. **92**, 680 (1990).
[17] V. Chirita, B. A. Pailthorpe, and R. E. Collins, J. Phys. D **26**, 133 (1993).
[18] R. J. W. E. Lahaye, A. W. Kleyn, S. Stolte, and S. Holloway, Surf. Sci. **338**, 169 (1995).
[19] R. J. W. E. Lahaye, S. Stolte, S. Holloway, and A. W. Kleyn, Surf. Sci. **363**, 91 (1996).
[20] T. Yan, W. L. Hase, and J. C. Tully, J. Chem. Phys. **120**, 1031 (2004).
[21] W. Brenig, Z. Phys. B **36**, 81 (1979).
[22] D. A. Micha, J. Chem. Phys. **74**, 2054 (1981).
[23] D. Kumamoto and R. Silbey, J. Chem. Phys. **75**, 5164 (1981).
[24] R. Brako, Surf. Sci. **123**, 439 (1982).
[25] B. Jackson, J. Chem. Phys. **88**, 1383 (1988); **92** 1458 (1990).
[26] J. R. Manson, Phys. Rev. B **43**, 6924 (1991).
[27] W. W. Hayes and J. R. Manson, J. Chem. Phys. **127**, 164714 (2007).
[28] J. R. Manson, in *Handbook of Surface Science*, edited by N. V. Richardson and S. Holloway (Elsevier, Amsterdam, 2008); *Surface Dynamics*, edited by E. Hasselbrink and B. Lundqvist, (Elsevier, Amsterdam, 2008), Vol. 3.
[29] E. Pollak, S. Sengupta, and S. Miret-Artés, J. Chem. Phys. **129**, 054107 (2008).
[30] E. Pollak and S. Miret-Artés, J. Chem. Phys. **130**, 194710 (2009).
[31] E. Pollak, J. M. Moix, and S. Miret-Artés (unpublished).
[32] C. Hättig and F. Weigend, J. Chem. Phys. **113**, 5154 (2000).
[33] C. Hättig and K. Hald, Phys. Chem. Chem. Phys. **4**, 2111 (2002).
[34] C. Hättig, A. Köhn, and K. Hald, J. Chem. Phys. **116**, 5401 (2002).
[35] R. Ahlrichs, M. Bär, H.-P. Baron, R. Bauernschmitt, S. Böcker, N. Crawford, P. Deglmann, M. Ehrig, K. Eichkorn, S. Elliott, F. Furche, F. Haase, M. Häser, C. Hättig, A. Hellweg, H. Horn, C. Huber, U. Huniar, M. Kattannek, A. Köhn, C. Kölmel, M. Kollwitz, K. May, P. Nava, C. Ochsenfeld, H. Öhm, H. Patzelt, D. Rappoport, O. Rubner, A. Schäfer, U. Schneider, M. Sierka, O. Treutler, B. Unterreiner, M. von Arnim, F. Weigend, P. Weis, and H. Weiss, TURBOMOLE, Version 6.0, Universität Karlsruhe, 2009.
[36] T. H. Dunning, Jr., J. Chem. Phys. **90**, 1007 (1989).
[37] D. E. Woon and T. H. Dunning, Jr., J. Chem. Phys. **98**, 1358 (1993).
[38] D. Andrae, U. Häußermann, M. Dolg, H. Stoll, and H. Preuss, Theor. Chim. Acta **77**, 123 (1990).
[39] F. Weigend and R. Ahlrichs, Phys. Chem. Chem. Phys. **7**, 3297 (2005).
[40] Y. Ralchenko, A. Kramida, J. Reader, and NIST ASD Team, NIST Atomic Spectra Database, Version 3.1.5. National Institute of Standards and Technology, Gaithersburg, MD, June 18 2009 (http://physics.nist.gov/asd3).
[41] Z. Ma and K. Balasubramanian, Chem. Phys. Lett. **181**, 467 (1991).
[42] C. Hättig, Phys. Chem. Chem. Phys. **7**, 59 (2005).
[43] A. Hellweg, C. Hättig, S. Höfener, and W. Klopper, Theor. Chem. Acc. **117**, 587 (2007).
[44] MOLPRO, a package of *ab initio* programs designed by H.-J. Werner and P. J. Knowles, version 2006.1, R. Lindh, F. R. Manby, M. Schütz *et al.*, see http://www.molpro.net
[45] B. O. Roos, R. Lindh, P.-Å. Malmqvist, V. Veryazov, and P.-O. Widmark, J. Phys. Chem. A **109**, 6575 (2005).
[46] M. Douglas and N. M. Kroll, Ann. Phys. (N.Y.) **82**, 89 (1974).
[47] B. A. Hess, Phys. Rev. A **33**, 3742 (1986).
[48] P. J. Knowles, C. Hampel, and H.-J. Werner, J. Chem. Phys. **99**, 5219 (1993).
[49] H.-J. Werner and P. J. Knowles, J. Chem. Phys. **82**, 5053 (1985).
[50] P. J. Knowles and H.-J. Werner, Chem. Phys. Lett. **115**, 259 (1985).
[51] S. F. Boys and F. Bernardi, Mol. Phys. **19**, 553 (1970).
[52] J. F. Garvey and A. Kuppermann, J. Phys. Chem. **92**, 4583 (1988).
[53] R. Car and M. Parrinello, Phys. Rev. Lett. **55**, 2471 (1985).
[54] N. L. Doltsinis and D. Marx, J. Theor. Comput. Chem. **1**, 319 (2002).
[55] H. B. Schlegel, Bull. Korean Chem. Soc. **24**, 1 (2003).
[56] A. Groß and A. Dianat, Phys. Rev. Lett. **98**, 206107 (2007).
[57] B. Gumhalter, Phys. Rep. **351**, 1 (2001).
[58] R. Guantes, A. S. Sanz, J. Margalef-Roig, and S. Miret-Artés, Surf. Sci. Rep. **53**, 199 (2004).
[59] J. M. Moix and E. Pollak, Phys. Rev. A **79**, 062507 (2009).